Mechanics of Materials 170 (2022) 104334

Contents lists available at ScienceDirect

Mechanics of Materials

journal homepage: www.elsevier.com/locate/mecmat

Research paper

A validated multiscale model linking microstructural features of fired clay brick to its macroscopic multiaxial strength

Thomas Buchner [a], Markus Königsberger [a,b], Andreas Jäger [c], Josef Füssl [a,*]

[a] Institute for Mechanics of Materials and Structures, TU Wien, Karlsplatz 13/202, 1040 Vienna, Austria
[b] BATir Department, Université libre de Bruxelles, CP194/04, 50 avenue F.D. Roosevelt, Brussels 1050, Belgium
[c] Wienerberger AG, Wienerbergerplatz 1, 1100 Vienna, Austria

ARTICLE INFO

Keywords:
Clay brick
Multiscale material model
Strength

ABSTRACT

Given the popularity of fired clay bricks in increasingly taller buildings, as well as the large variety of raw materials, additives, tempers, and production technology, microstructure-based modeling of the brick strength is essential. This paper aims at linking the microstructural features of bricks, i.e. the volume, shape, and size of mineral phases, pores, and the glassy binding matrix in between, to the multiaxial failure behavior of bricks. Therefore, a continuum micromechanics multiscale model, developed originally for stiffness and thermal conductivity upscaling, is adopted and complemented with a Mohr–Coulomb failure criterion at the microscale. By micromechanics-based downscaling of uniaxial brick strength tests, quantitative insights into the strength of the binding matrix are obtained for the first time. After successful nanoindentation-based validation of the identified micro-strength, the model is used for predicting the macroscopic multiaxial brick strength, which in turn is successfully validated against independent bi- and triaxial compressive strength test results.

1. Introduction

The mechanical strength of brick masonry is of paramount importance as it often is, together with the thermal conductivity, the critical aspect in construction design and planning. The popularity as economically and ecologically efficient building material has motivated the use of fired clay bricks for increasingly taller and increasingly more complex masonry constructions, such as multi-storey residential buildings, where the load-bearing capacity of masonry is pushed to its limit. The strength of masonry walls is often governed by brick failure (Ganz, 1985; Lourenço, 1997; Lourenço and Vasconcelos, 2015), more precisely by failure of the brick body in solid bricks or in the webs of customarily used perforated bricks. Even in simple vertically loaded walls, the brick body is subjected to complex multiaxial stress states. To assess the mechanical stability, construction engineers therefore require a suitable material model for multiaxial failure of bricks.

Modern bricks come in a huge variety. Different clays, mixed with different pore-forming additives (e.g. extruded polystyrene, sawdust, paper sludge) and different tempers (quartz, slag, fly-ash), are extruded through different molds and fired at different temperatures (ranging typically from 800–1200 °C), making it impossible to perform laboratory tests on each and every brick under each and every loading scenario, in order to assess its multiaxial failure behavior. Model predictions are therefore essential. In this context, numerical finite element (FE) models (Kiefer et al., 2017; Suda et al., 2021; Graubner and Richter, 2007; Nguyen and Meftah, 2014) have considerably advanced recently and can accurately predict the failure of extruded bricks based on a multiaxial failure behavior of the brick body. This paper deals with failure of the latter, which is, still either described only qualitatively (Müller et al., 2010, 2015; Kilikoglou et al., 1995, 1998) or modeled phenomenologically (D'Orazio et al., 2014; Wagh et al., 1993; Chapagain et al., 2020) by fitting the measured strength to compositional features such as porosity and/or temper volume fraction and temper shape. The limited predictive capabilities of these phenomenological models motivate a shift to microstructure-based strength models, fostered by continuously improving small-scale characterization techniques.

Morphometrical features (Krakowiak et al., 2011; Allegretta et al., 2017; Coletti et al., 2016a,b; Kariem et al., 2018, 2020b; Buchner et al., 2021c,a) as well as mechanical (Krakowiak et al., 2011; Kariem et al., 2020a) properties of the brick microstructure have been deciphered within the last two decades. The emerging microstructural image of bricks shows that nano- to micrometer-sized pores as well crystalline mineral grains (mostly quartz, feldspar, and mica) are distributed randomly but oriented preferably along the extrusion direction. The minerals are "glued" together by a stiff glassy matrix-like constituent which, driven by the extrusion pressure, itself is anisotropic. Understanding

* Corresponding author.
E-mail address: josef.fuessl@tuwien.ac.at (J. Füssl).

https://doi.org/10.1016/j.mechmat.2022.104334
Received 2 March 2022; Accepted 25 April 2022
Available online 10 May 2022

the link between these microstructural features and the macroscopic properties is the key for predicting the brick performance. Microstructural features have already been successfully linked to the macroscopic stiffness as well as the macroscopic thermal conductivity based on analytical multiscale approaches (Pichler et al., 2015; Pabst and Gregorová, 2007, 2017; Pabst and Uhlířová, 2021; Živcová et al., 2009a,b; Kiefer et al., 2020; Buchner et al., 2021b) or numerical multiscale models (Grandjean et al., 2006; Uhlířová et al., 2018; Hříbalová et al., 2021). Similar microstructure-based links for strength are, however, still missing, a micro-to-macro gap tackled to be bridged herein.

Motivated by the already successful application of continuum micromechanics models to predict the elastic limit or strength of cement paste (Pichler and Hellmich, 2011), concrete (Königsberger et al., 2014a,b, 2018; Königsberger and Staquet, 2018), lime-based mortar (Nežerka et al., 2017), and wood (Bader et al., 2010; Hofstetter et al., 2008; Gangwar and Schillinger, 2019), we herein aim at extending the micromechanics model developed for stiffness and conductivity homogenization of fired clay bricks (Buchner et al., 2021b) towards failure modeling. Continuum micromechanics modeling (Hill, 1963; Zaoui, 2002) is, on the one hand, able to incorporate the microstructural features in suitable detail (almost matching numerical FE approaches), but on the other hand, computationally efficient and robust given its analytical nature. Thereby, the macroscopic properties are obtained from upscaling of morphometric (volume, shape, size) features and mechanical properties of the individual constituents, which are considered to interact at distinct observation scales.

The remainder of the paper is structured as follows. In Section 2, the micromechanics representation of brick (Buchner et al., 2021b) is revisited and complemented with a failure criterion at the microscale. The required morphometric, elastic, and strength properties of the solid constituents (mineral phases and glassy matrix) of bricks are discussed in Section 3. Section 4 is devoted to comprehensive model validation attempts, at both the microscale and the macroscale. To corroborate the considered microscale strength criterion and its constants, it is incorporated into a finite element (FE) model to analyze a nanoindentation test performed by Kariem et al. (2020a). To corroborate the predicted macroscopic brick strength, model predictions are compared to published test results from multiaxial compression tests. The paper is closed with a summary, concluding remarks and an outlook (Section 5).

2. Multiscale micromechanics model for brick failure

2.1. Micromechanical representation

Extruded and fired clay brick is considered in the framework of continuum micromechanics (Hill, 1963; Suquet, 1997; Zaoui, 2002; Dormieux et al., 2006) as a macro-homogeneous, but micro-heterogeneous body built up by two representative volume elements (RVEs) at two observation scales (Buchner et al., 2021b), see Fig. 1. The RVE at scale s with characteristic size l_s is built up by homogeneous material phases with characteristic size d_s, with scale-specific phase volume fractions f_p^s, and with constant mechanical properties. At the mesoscale, the RVE characteristically measures $l_{\text{meso}} = 300$ μm and is built up by mineral grains (quartz, feldspar, muscovite, and Fe–Mg mica) and mesopores with characteristic sizes $d_{\text{meso}} \leq 150$ μm, which are embedded in a foam matrix. The heterogeneity of the foam matrix is resolved at the microscale, with characteristic RVE size amounting to $l_{\text{micro}} = 3$ μm, and consists of a binding matrix hosting micropores (with characteristic sizes $d_{\text{micro}} \leq 1$ μm).

The RVEs fulfill the scale separation conditions

$$\left.\begin{aligned} d_{\text{micro}} \leq 1\ \mu\text{m} \ll l_{\text{micro}} = 3\ \mu\text{m} \lll \\ d_{\text{meso}} \leq 150\ \mu\text{m} \ll \end{aligned}\right\} l_{\text{meso}} = 300\ \mu\text{m} \lll \mathcal{L} = 15\ \text{mm} \tag{1}$$

with $\mathcal{L} = 15$ mm as the characteristic size of the brick, and with much larger symbols "$\ll$" referring to factors of only 2–3 (Drugan and Willis, 1996) and very much larger symbols "$\lll$" referring to factors of 10 (Kohlhauser and Hellmich, 2013).

All inclusion-type material phases are considered as oblate spheroids with aspect ratios $X_p = a_{p,\bar{x}}/a_{p,\bar{z}}$, whereby $a_{p,\bar{x}}$ and $a_{p,\bar{z}}$ denote the axes lengths of the spheroid, see Fig. 1(b). The extrusion pressure in thickness direction z causes a preferential orientation of all inclusion-type material phases along the x–y-plane (Krakowiak et al., 2011; Bartusch and Händle, 2007; Bourret et al., 2015; Buchner et al., 2021a), whereby the x-direction coincides with extrusion direction, see Fig. 1(a). The orientations are quantified by means of a symmetric (with respect to the x–y-plane) orientation distribution function $W_p(\theta) = \kappa_p \cdot \cosh(\kappa_p \cos(\theta))/\sinh(\kappa_p)$, with κ_p denoting the scalar parameter of the distribution, see Fig. 1(c), and with θ as the zenith angle between the global z-axis and the local $\bar{z}$-axis. The orientation distribution along the azimuth angle φ is considered uniform.

2.2. Mohr–Coulomb failure at the binding matrix

We consider that brick failure at the macroscale is triggered by failure of the binding matrix at the microscale. Given the granular texture of the binding matrix in the sub-micron range at the present firing temperature, see Krakowiak et al. (2011), we consider its failure to be of cohesive-frictional nature, which is modeled by means of a Mohr–Coulomb criterion reading as

$$f_{MC}(\boldsymbol{\sigma}_{\text{bm}}) = \sigma_{\text{bm},I}\frac{1+\sin\varphi_{\text{bm}}}{2c_{\text{bm}}\cos\varphi_{\text{bm}}} - \sigma_{\text{bm},III}\frac{1-\sin\varphi_{\text{bm}}}{2c_{\text{bm}}\cos\varphi_{\text{bm}}} - 1\ , \tag{2}$$

with $\sigma_{\text{bm},I}$ denoting the maximum and $\sigma_{\text{bm},III}$ denoting the minimum principal normal stress in the binding matrix, c_{bm} as cohesion, and φ_{bm} as angle of internal friction. The binding matrix, and thus the brick, resists as long as $f_{MC} < 0$, microscopic and macroscopic failure occurs as soon as $f_{MC} = 0$.

2.3. Macro-to-micro stress downscaling

Evaluation of the proposed microscale failure criterion Eq. (2) requires quantification of the failure-inducing binding matrix stresses $\boldsymbol{\sigma}_{\text{bm}}$. Herein, we consider *spatial average* stresses of the binding matrix as suitable for modeling failure. These stresses are obtained from macroscopic stresses $\boldsymbol{\Sigma}$ applied on a piece of brick by an elastic (linear) macro-to-micro stress concentration ("stress downscaling") rule in the framework of continuum micromechanics (Zaoui, 2002), reading as

$$\boldsymbol{\sigma}_{\text{bm}} = \mathbb{B}_{\text{bm}} : \boldsymbol{\Sigma}\ . \tag{3}$$

with $\mathbb{B}_{\text{bm}}$ as fourth-order phase stress concentration tensor.

Access to the sought stress concentration tensor $\mathbb{B}_{\text{bm}}$ is provided by the envisioned linear elastic phase behavior linking phase strains $\boldsymbol{\varepsilon}_p$ to phase stresses $\boldsymbol{\sigma}_p$ via the phase stiffness $\mathbb{C}_p$, by its macroscopic counterpart $\boldsymbol{E} = (\mathbb{C}_{\text{brick}})^{-1} : \boldsymbol{\Sigma}$ with $\mathbb{C}_{\text{brick}}$ as homogenized brick stiffness, and by RVE-specific linear strain concentration relations allowing us to concentrate macrostrains to strains in the foam matrix, $\boldsymbol{\varepsilon}_{\text{fm}} = \mathbb{A}_{\text{fm}} : \boldsymbol{E}$, and further down to strains in the binding matrix, $\boldsymbol{\varepsilon}_{\text{bm}} = \mathbb{A}_{\text{bm}} : \boldsymbol{\varepsilon}_{\text{fm}}$; whereby $\mathbb{A}_p$ is the fourth-order phase strain concentration tensor. Combination of the aforementioned strain concentration relations with the constitutive relations and comparison to stress concentration rule (3) allows us to rewrite the stress concentration tensor $\mathbb{B}_{\text{bm}}$ as

$$\mathbb{B}_{\text{bm}} = \mathbb{C}_{\text{bm}} : \mathbb{A}_{\text{bm}} : \mathbb{A}_{\text{fm}} : (\mathbb{C}_{\text{brick}})^{-1}\ . \tag{4}$$

$\mathbb{C}_{\text{brick}}$ is the homogenized stiffness of the RVE at the mesoscale, $\mathbb{C}_{\text{brick}} = \mathbb{C}_{\text{hom}}^{\text{meso}}$, and it is obtained from consecutive Mori–Tanaka (Mori and Tanaka, 1973; Benveniste, 1987) stiffness homogenization at micro- and mesoscale, where the homogenized elastic stiffness tensor $\mathbb{C}_{\text{hom}}^{s}$

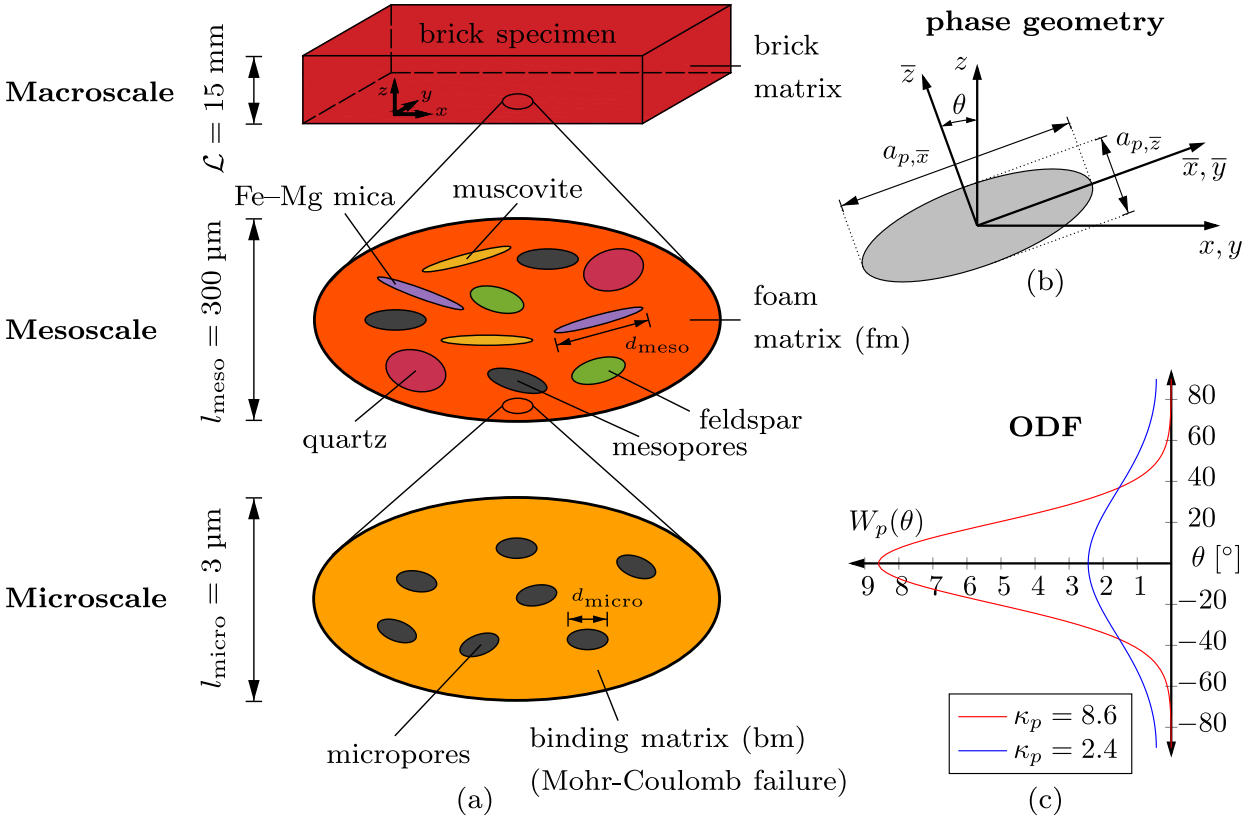

Fig. 1. (a) Two-scale micromechanics material model for fired clay brick (macroscale) adopted from Buchner et al. (2021b): mesoscale with foam matrix (homogenized at microscale), mineral phases, and mesopores; microscale with binding matrix and micropores. Mineral and pore phases are modeled as (b) oblate spheroids with aspect ratios $X_p = a_{p,\overline{x}}/a_{p,\overline{z}}$ and with (c) orientation distributions function (ODF) $W_p(\theta)$ along the zenith angle θ, while the orientation distribution along the azimuth angle φ is uniform.

of scale $s \in \{\text{micro}, \text{meso}\}$ reads as (Zaoui, 2002; Königsberger et al., 2020; Buchner et al., 2021b)

$$\mathbb{C}^s_{\text{hom}} = \sum_r f^s_r \int_0^{\pi} W_r(\theta) \int_0^{2\pi} \mathbb{C}_r : \mathbb{A}_r(\varphi, \theta; X_r) \mathrm{d}\varphi \frac{\sin(\theta)}{4\pi} \mathrm{d}\theta \,, \tag{5}$$

with f^s_p as volume fraction of phase p. The phase strain concentration tensors $\mathbb{A}_p$ follow from matrix-inclusion problems (Eshelby problems Eshelby, 1957), where a single inclusion is embedded in and perfectly bonded to an infinite matrix, and reads as (Zaoui, 2002; Königsberger et al., 2020; Buchner et al., 2021b)

$$\begin{aligned}\mathbb{A}_p(\overline{\varphi}, \overline{\theta}; X_p) = [\mathbb{I} + \mathbb{P}_p(\overline{\varphi}, \overline{\theta}; X_p) : (\mathbb{C}_p - \mathbb{C}_m)]^{-1} \\ : \left[\sum_r f^s_r \int_0^{\pi} W_r(\theta) \int_0^{2\pi} [\mathbb{I} + \mathbb{P}_r(\varphi, \theta; X_r) : (\mathbb{C}_r - \mathbb{C}_m)]^{-1} \right. \\ \left. \times \, \mathrm{d}\varphi \frac{\sin(\theta)}{4\pi} \mathrm{d}\theta \right]^{-1} ,\end{aligned} \tag{6}$$

with $\mathbb{P}_p$ denoting the fourth-order Hill tensor (see Mura (1987) and Hill (1965) for tensor components), and $\mathbb{I}$ denoting the fourth-order identity tensor defined as $I_{ijkl} = 1/2(\delta_{ik}\delta_{jl} + \delta_{il}\delta_{jk})$ with δ_{ij} as Kronecker delta. Homogenization at the microscale requires the evaluation of Eqs. (5) and (6) for the material phases $p, r \in \{\text{bm}, \text{micropores}\}$ and $\mathbb{C}_m = \mathbb{C}_{\text{bm}}$. Homogenization at mesoscale, in turn, requires the consideration of material phases $p, r \in \{\text{fm}, \text{mesopores}, \text{quartz}, \text{feldspar}, \text{muscovite}, \text{Fe–Mg mica}\}$ and $\mathbb{C}_m = \mathbb{C}_{\text{fm}} = \mathbb{C}^{\text{micro}}_{\text{hom}}$, see Fig. 1. Notably, integration along the surface of a unit sphere in Eqs. (5) and (6) is necessary due to the non-uniform phase orientation distributions $W_p(\theta)$. Thus, azimuth angle φ and zenith angle θ run along the unit sphere's surface, and $\overline{\varphi}, \overline{\theta}$ represent fixed orientation angles. On account of spheroidal inclusion geometries and transversal isotropic phase stiffnesses, as given in Section 3.1, the applied Mori–Tanaka scheme leads to a non-symmetric brick stiffness tensor $\mathbb{C}_{\text{brick}}$. Symmetrization of this tensor, $\mathbb{C}_{\text{brick}} = \left[\mathbb{C}_{\text{brick}} + (\mathbb{C}_{\text{brick}})^T\right]/2$, provides a very accurate approximation of the symmetric Mori–Tanaka scheme according to Sevostianov and Kachanov (2014), see also Buchner et al. (2021b) for more details.

3. Material characteristics

3.1. Phase morphometry

The model is evaluated for a typical calcareous clay brick fired at 880 °C,[1] which microstructure, chemical and mineralogical composition were investigated by Kariem et al. (2018, 2020a,b). The phase volume fractions related to the mesoscale f^{meso}_p, aspect ratios X_p, and orientation distribution parameters κ_p of all material phases were investigated using scanning electron microscopy coupled with energy dispersive X-ray spectroscopy, and subsequent image analysis, see Table 1 and Buchner et al. (2021b) for numerical values. The microscale-related volume fractions are calculated as $f^{\text{micro}}_{\text{bm}} = f^{\text{meso}}_{\text{bm}}/f^{\text{meso}}_{\text{fm}}$ and $f^{\text{micro}}_{\text{micropores}} = f^{\text{meso}}_{\text{micropores}}/f^{\text{meso}}_{\text{fm}}$ with $f^{\text{meso}}_{\text{fm}} = f^{\text{meso}}_{\text{bm}} + f^{\text{meso}}_{\text{micropores}}$.

3.2. Phase stiffness

Phase stiffness tensors $\mathbb{C}_p$ are given in terms of phase compliance tensors $\mathbb{D}_p = (\mathbb{C}_p)^{-1}$ with respect to the local base frame $(\overline{x}, \overline{y}, \overline{z})$ in

[1] The brick is labeled F in Buchner et al. (2021b) who analyzed its thermal conductivity and stiffness.

Table 1
Experimentally-identified morphometry parameters (mesoscale-related volume fractions f_p^{meso}, aspect ratios X_p, and orientation distribution parameters κ_p) and elasticity constants (Young's moduli $E_{p,\bar{x}} = E_{p,\bar{y}}$ and $E_{p,\bar{z}}$, Poisson's ratio ν_p) of all considered material phases.

	f_p^{meso} [%]	X_p [–]	κ_p [–]	$E_{p,\bar{x}} = E_{p,\bar{y}}$ [GPa]	$E_{p,\bar{z}}$ [GPa]	ν_p [–]
micropores	10	4.82	3.80	0	0	–
mesopores	26	4.82	3.80	0	0	–
quartz < 10 μm	5	3.09	2.96	113.3	80.8	0.077
quartz > 10 μm	11	3.09	2.96	0	0	–
feldspar	9	3.40	4.88	81.2	60.9	0.290
muscovite	7	9.86	6.08	62.0	35.5	0.249
Fe–Mg mica	2	10.83	12.29	60.0	37.7	0.288
binding matrix	30	–	–	62.5	45.8	0.200

Kelvin–Mandel notation as

$$\mathbb{D}_p = \left(\mathbb{C}_p\right)^{-1} = \begin{bmatrix} \frac{1}{E_{p,\bar{x}}} & \frac{-\nu_p}{E_{p,\bar{x}}} & \frac{-\nu_p}{E_{p,\bar{z}}} & 0 & 0 & 0 \\ \frac{-\nu_p}{E_{p,\bar{x}}} & \frac{1}{E_{p,\bar{x}}} & \frac{-\nu_p}{E_{p,\bar{z}}} & 0 & 0 & 0 \\ \frac{-\nu_p}{E_{p,\bar{z}}} & \frac{-\nu_p}{E_{p,\bar{z}}} & \frac{1}{E_{p,\bar{z}}} & 0 & 0 & 0 \\ 0 & 0 & 0 & \frac{1}{2G_{p,\bar{x}\bar{z}}} & 0 & 0 \\ 0 & 0 & 0 & 0 & \frac{1}{2G_{p,\bar{x}\bar{z}}} & 0 \\ 0 & 0 & 0 & 0 & 0 & \frac{1}{2G_{p,\bar{x}\bar{y}}} \end{bmatrix}_{\bar{x},\bar{y},\bar{z}} . \quad (7)$$

whereby three independent quantities are considered, two independent moduli $E_{p,\bar{x}} = E_{p,\bar{y}}$ and $E_{p,\bar{z}}$ and a single value for the Poisson's ratio ν_p, and whereby $G_{p,\bar{x}\bar{y}} = \frac{E_{p,\bar{x}}}{2(1+\nu_p)}$ and $G_{p,\bar{x}\bar{z}} = \frac{E_{p,\bar{x}}+E_{p,\bar{z}}}{4(1+\nu_p)}$, see Buchner et al. (2021b) for more details on the underlying assumptions. The elastic constants of all mineral phases are compiled in Table 1. Phase moduli were adopted from a grid nanoindentation study performed by Kariem et al. (2020a). The Poisson's ratios of inclusion-type mineral phases were adopted from ultrasound measurements by Christensen (1996), and the Poisson's ratio of binding matrix is assumed to 0.20, inspired by the Poisson's ratio of glass according to Buchner et al. (2021b). Notably, we distinguish between quartz grains with diameter <10 μm, which exhibit typical quartz stiffness, and grains with diameter >10 μm. Large quartz grains very often show cracks along or close to their boundaries, which are induced by an erratic volume decrease of quartz during cooling, more precisely, during the transformation of β- to α-quartz at 573 °C (Kilikoglou et al., 1998; Müller et al., 2010). In the model, quartz (diameter >10 μm) is assumed to entirely loose the contact to the surrounding matrix, which is why the stiffness of all quartz grains >10 μm is considered to vanish, see Table 1.

3.3. Phase strength: Back-identification of cohesion and friction angle

To complete the model, quantification of the Mohr–Coulomb failure constants of the binding matrix (cohesion c_{bm} and angle of internal friction φ_{bm}) is necessary. Direct experimental access, however, is out of reach, given the lack of reliable small-scale experimental techniques for the determination of the material strength. As a remedy, we aim at their identification from macroscopic tensile and compressive strength tests, as described next.

The tensile strength was approximated as the maximum cross-sectional stress Σ_{xx} in a three-point bending test on a specimen measuring 125×30×15 mm with x-direction coinciding the extrusion direction, see the scheme in Fig. 2(a). Applying Bernoulli's beam theory, the maximum stress in the cross section at failure reads as $f_{t,x} = 3F_{max}l/(2bh^2)$, with $b = 30$ mm as horizontal and $h = 15$ mm as vertical cross-sectional dimension, respectively, $l = 50$ mm as distance between the two bearings, and F_{max} as peak load. Mean value and standard deviation of the tensile strength f_t were obtained from 12 single experiments and amount to $f_{t,x} = 23.10 \pm 1.60$ MPa.

The compressive strength was determined by means of uniaxial compression tests on extruded vertically perforated brick specimens measuring 50 × 25 × 25 mm, see Fig. 2(b). The perforation of 30% of the cross-sectional area A_{tot} increases the specimen slenderness of the webs, which renders the influence of friction-induced shear stresses negligible, at least in the central region of the brick where failure is initiated. To ensure a uniform load transmission from the testing machine to the specimen, the top and bottom surfaces were carefully ground. Through dividing the applied force at peak load, F_{max}, by the net cross section $A_{net} = 0.7A_{\text{tot}}$, the compressive strength amounts to $f_{c,x} = F_{max}/A_{net} = 74.29 \pm 5.07$ MPa, whereby mean value and standard deviation were obtained from 16 single experiments.

Finally, the strength test results are downscaled to the binding matrix level. Therefore, the macroscopic stress states at failure in the three-point bending test and the uniaxial compression test read as $\boldsymbol{\Sigma}^t = f_{t,x}\boldsymbol{e}_x \otimes \boldsymbol{e}_x$ and $\boldsymbol{\Sigma}^c = -f_{c,x}\boldsymbol{e}_x \otimes \boldsymbol{e}_x$, respectively, with the unit vector $\boldsymbol{e}_x = (1\ 0\ 0)^T$ pointing in extrusion direction. The corresponding microstresses in the binding matrix ($\boldsymbol{\sigma}^t_{\text{bm}}$, $\boldsymbol{\sigma}^c_{\text{bm}}$), are readily obtained from evaluation of stress downscaling Eq. (3). Inserting $\boldsymbol{\sigma}^t_{\text{bm}}$ and $\boldsymbol{\sigma}^c_{\text{bm}}$, respectively, into the Mohr–Coulomb failure function $f_{MC}(\boldsymbol{\sigma}_{\text{bm}})$ according to Eq. (2), and setting $f_{MC} = 0$ results in two algebraic equations, which allow for the identification of the two sought Mohr–Coulomb constants, yielding $c_{\text{bm}} = 37.59$ MPa and $\varphi_{\text{bm}} = 33.14°$.

4. Multiscale model validation and discussion

4.1. Nanoindentation-based validation of the binding matrix failure

4.1.1. Strategy

We herein aim at the validation of the envisioned Mohr–Coulomb-type failure behavior of the binding matrix including the two back-identified failure constants (c_{bm} and φ_{bm}). Therefore, we rely on nanoindentation tests in combination with numerical modeling. The response of a material to indentation experiments is well known to correlate with the material strength, as shown e.g. for steel (Brinell, 1901; Williams, 1942; Tabor, 1951) and for cementitious materials (Ganneau et al., 2006; Igarashi et al., 1996; Constantinides et al., 2003; Kholmyansky et al., 1994). Given the complex stress field below the indenter tip, numerical approaches based on the finite elements (FE) have been developed more recently (Sarris and Constantinides, 2013; Chen et al., 2006; Kermouche et al., 2008; Zhang et al., 2006b,a), to quantitatively link the indentation test-related force–displacement behavior to the material strength. Extending this modeling idea to our brick material, we aim at (i) predicting the load–displacement curve for nanoindentation in the binding matrix using FE simulations based on the implied Mohr–Coulomb failure behavior, (ii) comparing the FE predictions to measured load–displacement curves, and (iii) this way validating the binding matrix properties.

4.1.2. Nanoindentation tests

Kariem et al. (2020a) performed nanoindentation experiments on the very same bricks as studied herein. The material was indented in extrusion direction x as well as thickness direction z using a TI900 Tribo-indenter (Hysitron, USA) with a Berkovich tip (three-sided pyramid) with fillet radius of 100 nm. The authors executed load-controlled grid nanoindentations (33 × 23 indents) with two load cycles at each indent, the first one to anticipate plastic deformations and the second one to obtain viscoelastic material properties. The load protocol, depicted in Fig. 3, consisted of fast loading in 0.2 s up to 280 μN followed by unloading in 0.2 s and a holding phase of 10 s with 2 μN load. Thereafter, the load was increased to 250 μN within 0.3 s, held for 20 s followed by unloading to 2 μN within 0.3 s and a final holding phase of 15 s. We focus solely on the very short first load cycle in order to eliminate most of the viscose effects.

Indents in the binding matrix are isolated from the 33 × 23 = 759 measurements in x and the 759 measurements in z-direction as follows:

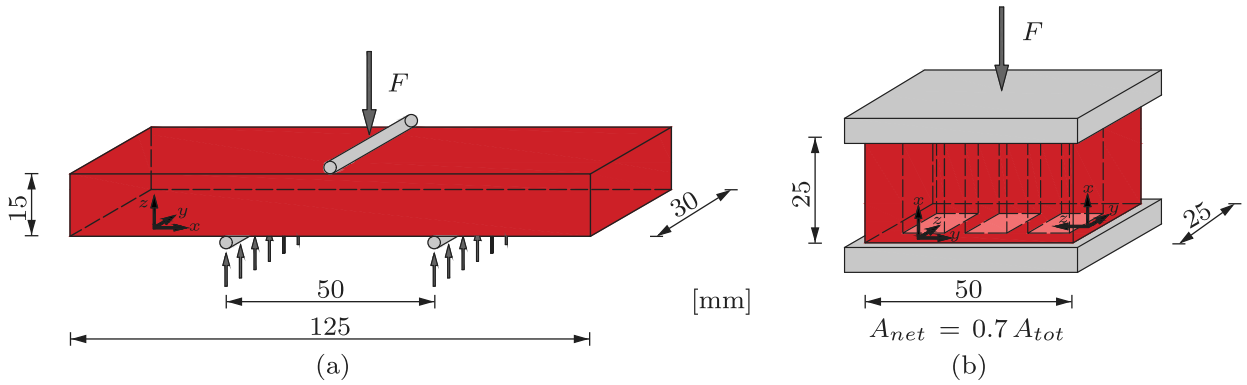

Fig. 2. Macroscopic strength tests: (a) three-point bending, (b) uniaxial compression.

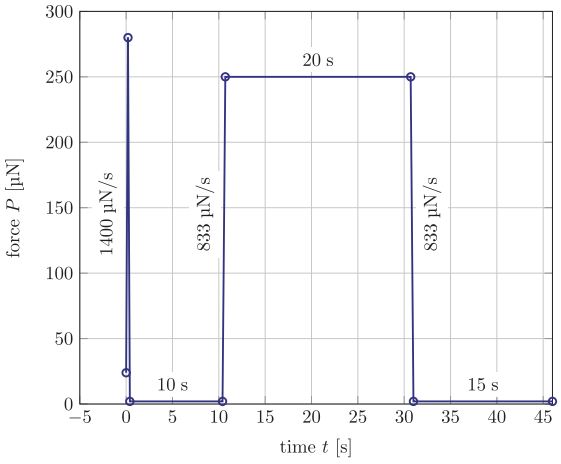

Fig. 3. Load function applied for nanoindentation experiments by Kariem et al. (2020a).

All indents, that refer to reduced elastic moduli within an interval of ±3 GPa from the average amounting to $E_{x,r} = 61.6$ GPa in x-direction and $E_{z,r} = 45.8$ GPa in z-direction, are assigned to the binding matrix resulting in roughly 40 characteristic indents in each direction, see Fig. 4 for the 40 individual displacement–time responses, together with averages (thick lines). Notably, the elastic moduli of the binding matrix as well as of the other microstructural phases were obtained according to the evaluation method of Oliver and Pharr (1992, 2004), and thus are an input for the micromechanical model, see Section 3.2.

4.1.3. Finite element model

A 2D-axisymmetric FE model is developed using the commercial FE software ABAQUS (Dassault Systèmes, France), see Fig. 5. Therefore, the diamond indenter tip is modeled as cone with half apex angle $\theta = 70.3°$, giving the same projected area as the Berkovich tip, a simplification already used by Sarris and Constantinides (2013). The tip radius amounts to 100 nm, matching the one reported in the experimental study (Kariem et al., 2018). The indenter is subjected to an area load which resultant linearly increases to 280 µN followed by linear unloading.

The material to be indented is represented geometrically by a cylindrical domain with 40 µm diameter and 40 µm height, see Fig. 5(a). Thus, the material domain is by almost three orders of magnitude larger than the indentation depth amounting to roughly 50 nm, which renders the effects of the boundary conditions on the modeling results negligible. The domain size is also much larger than the characteristic size of binding matrix phase at the microscale RVE in Fig. 1(a), which is considered to amount to 1 µm. Therefore, we consider the FE modeled material domain inhomogeneous in accordance with the envisioned multiscale micromechanics representation. In more detail, the binding matrix is represented as a hemispherical domain with radius of 0.5 µm, and is embedded into a hemispherical foam matrix domain (radius 1.5 µm), which in turn is embedded into a brick matrix domain, see Fig. 5(b).

As for discretization, 8-node biquadratic axisymmetric quadrilateral (CAX8) and 6-node quadratic axisymmetric triangle (CAX6) elements are used. The element size is continuously refined from 1 µm along the fixed (bottom and right) boundary down to 3 nm in the region close to the indenter tip. Mesh insensitivity was carefully analyzed.

The diamond tip is modeled as isotropic with elastic stiffness $E_i = 1140$ GPa and $\nu_i = 0.07$ (Oliver and Pharr, 2004). Brick, foam, and binding matrix are transversely isotropic materials (see Section 2.1). However, for FE modeling, we enforce the stiffness of all domains to be isotropic by considering a single Young's modulus E_p^* accompanied with a single Poisson's ratio ν_p^* in order to maintain the axissymmetry of the FE model. To compensate this simplification, we study the following two cases:

1. To model the indentation test in x-direction, the material-specific (single) modulus in the FE model is considered to be identical to the homogenized material-specific modulus in x-direction, $E_p^* = E_{p,x}$, and the Poisson's ratio is considered as $\nu_p^* = \nu_{p,xy}$. Given that $E_{p,x} > E_{p,z}$ (see Table 2 for the micromechanics-based results), this assumption refers to upper stiffness bounds of the indented materials and consequently to a lower bound for the sought displacement.
2. To model the indentation test in z-direction, we consider the much smaller modulus in z-direction as isotropic modulus, $E_p^* = E_{p,z}$, and moreover that $\nu_p^* = \nu_{p,xz}$. This case refers to lower stiffness bounds of the indented materials and consequently to an upper bound for the sought displacement.

Diamond indenter, foam matrix and brick matrix are considered to be purely (linear) elastic. The binding matrix is modeled as elasto-plastic material with a failure surface according to the Mohr–Coulomb criterion (2) with identified constants $c_{bm} = 37.59$ MPa and $\varphi_{bm} = 33.14°$. For the plastic potential, a smooth Menétrey–Willam surface (Menétrey and Willam, 1995) is considered and fitted as close as possible (without running into computational issues) to the Mohr–Coulomb failure surface in order to mimic associated plasticity.

Finally, friction at the interface between indenter and indented material is discussed. Experimental determination of the friction behavior is out of reach. As a remedy, we rely on results from FE-based sensitivity analysis of Sarris and Constantinides (2013). Assuming Coulomb-type friction in the interface, the authors showed that material pile-up around the indenter tip decreases significantly when increasing the friction coefficient, while the modeled load–displacement curves are

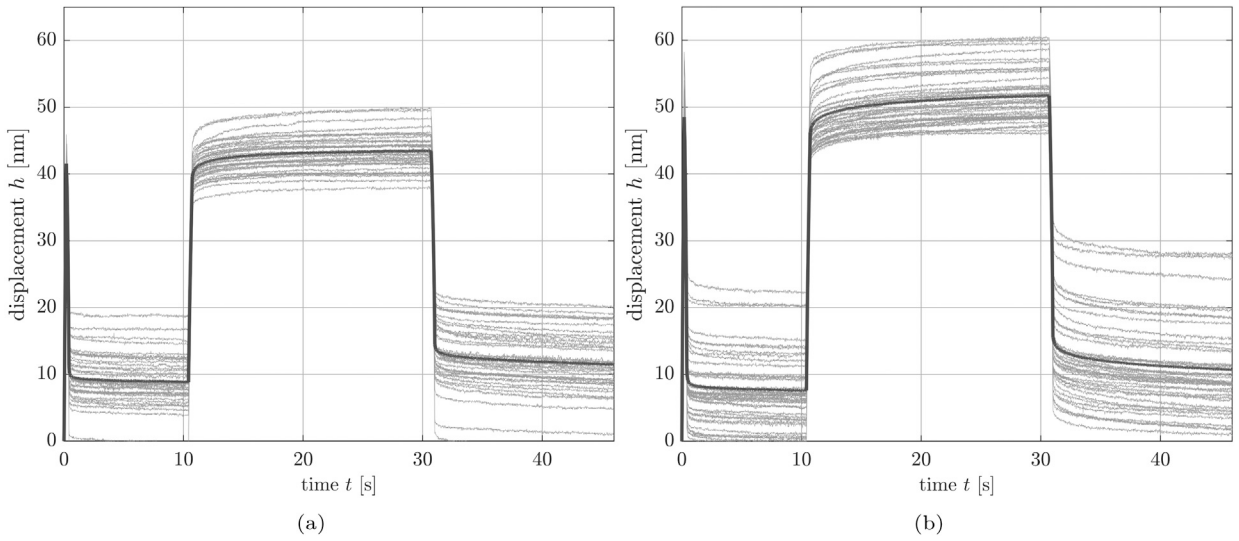

Fig. 4. Displacement–time diagrams of indents in the binding matrix reported by Kariem et al. (2018) in (a) x-direction and (b) z-direction with averages represented by thick lines.

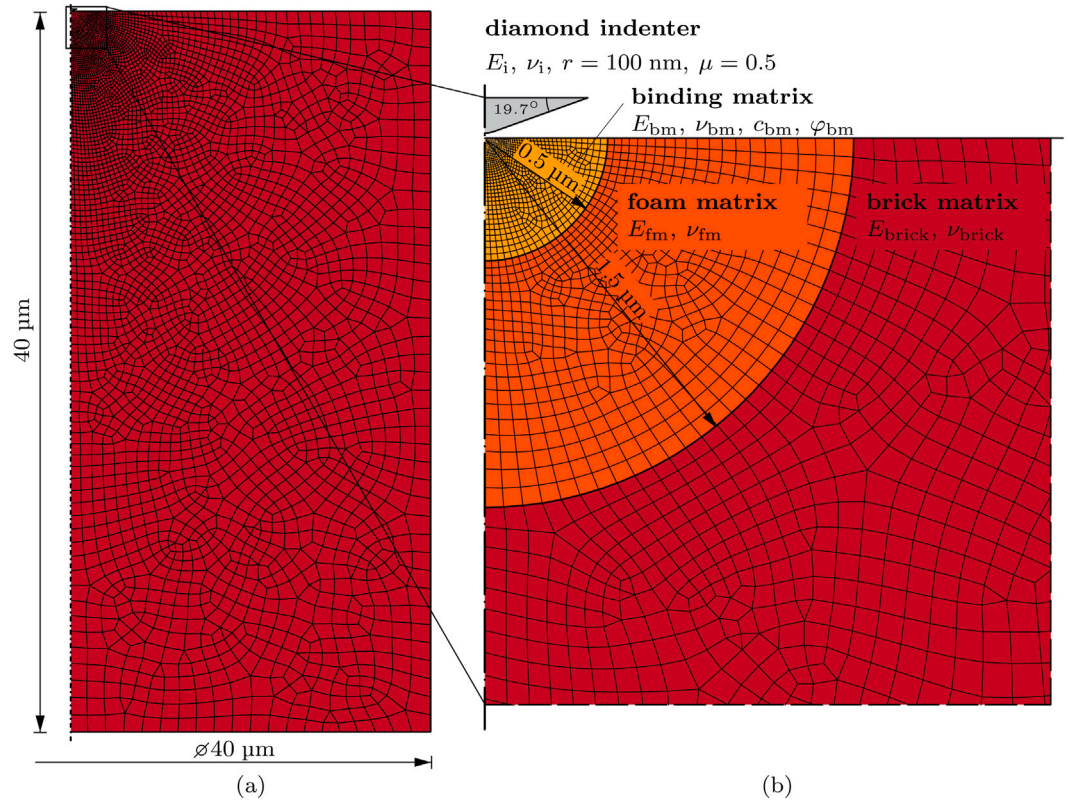

Fig. 5. 2D axisymmetric FE model of nanoindentation test with conical indenter and inhomogeneous cylindrical material domain discretized by CAX6 and CAX8 elements with sizes ranging from 1 µm along the fixed (bottom and right) boundary to 3 nm at the indent: (a) whole cylindrical domain with both height and diameter amounting to 40 µm; (b) detail of the inhomogeneous material domain with a binding matrix hemisphere embedded in a foam matrix hemisphere, which, in turn, is embedded in the brick matrix cylinder according to the characteristic sizes introduced in the micromechanics multiscale representation of Fig. 1(a).

virtually unaffected. Seeking for the latter, we simply adopt a typical friction coefficient amounting to 0.5.

Evaluating the FE model reveals significant permanent deformations after unloading with significant pile-up around the imprint, see Fig. 6(a). Plastic zones are rather localized, see Fig. 6(b), which confirms our ad-hoc assumption that failure is only possible within the one micron large inner hemisphere representing the binding matrix.

4.1.4. Comparison and validation

Experimentally measured force–displacement curves ($P - h$ curves) in x- and z-direction are compared to the model-predicted bounds next. Notably, loading paths in nanoindentation tests are significantly affected by contact uncertainties, e.g. contact force settings of the testing machine and slip. This uncertainty may likely lead to the large scatter in the loading branches of the 40 isolated force–displacement

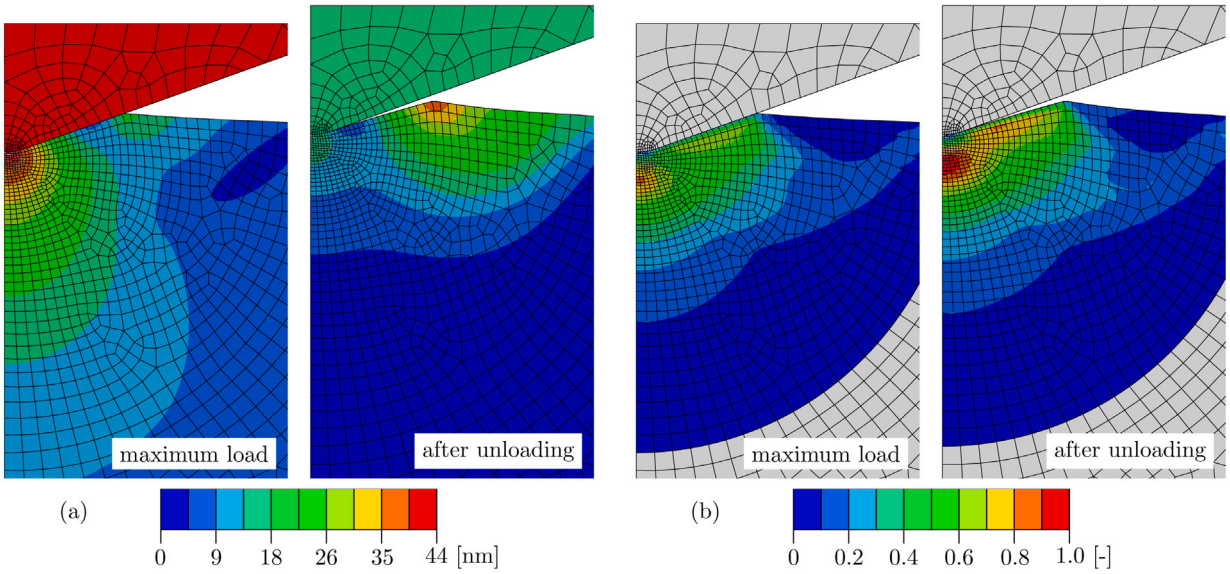

Fig. 6. FE modeling results at maximum load and after unloading for indentation in x-direction (upper stiffness bound): (a) displacement magnitude and (b) equivalent plastic strain.

Table 2
Isotropic elastic constants (Young's modulus E_p^* and Poisson's ratio ν_p^*) of matrix domains used for FE simulation of intentation tests in x-direction (first row) and z-direction (second row).

	E_{bm} [a] [GPa]	ν_{bm} [a] [–]	E^*_{fm} [b] [GPa]	ν^*_{fm} [b] [–]	E^*_{brick} [c] [GPa]	ν^*_{brick} [c] [–]
x-direction	62.50	0.20	35.08	0.18	17.85	0.18
z-direction	45.80	0.20	19.32	0.14	7.46	0.12

[a]From nanoindentation test in binding matrix from Kariem et al. (2020a), see also Table 1.
[b]From micromechanical homogenization of the microscale stiffness $\mathbb{C}_{\text{fm}} = \mathbb{C}^{\text{micro}}_{\text{hom}}$.
[c]From micromechanical homogenization of the mesoscale stiffness $\mathbb{C}_{\text{brick}} = \mathbb{C}^{\text{meso}}_{\text{hom}}$.

diagrams, see Fig. 7(a,b). The unloading branches, however, are rather parallel. As a consequence, and also in accordance with previous studies (VanLandingham et al., 2001), we only consider the unloading path (of the first load cycle) for validation purposes. Moreover, we initialize the measured and predicted displacements h by the maximum displacement at the (first) peak, h_{max}, to define the *unloading distance* $h_{\text{unl}} = h_{\text{max}} - h$, which will be further used for comparison.

Experimentally measured (average) and model-predicted unloading branches of the force-unloading distance curves ($P - h_{\text{unl}}$) are now compared to each other. Both experimentally measured $P - h_{\text{unl}}$ curves nicely fall within the model-predicted $P - h_{\text{unl}}$ range (hatched domain) between the two modeled cases, see Fig. 7(c). Moreover, the measured $P - h_{\text{unl}}$ curve obtained from indenting in the stiff extrusion direction (x-direction) is close to the model-predicted $P - h_{\text{unl}}$ curve for the case $E_p^* = E_{p,x}$, i.e. when the homogenized modulus in x-direction is considered representative for the isotropic modulus in the FE model. A small underestimation of the permanent unloading distance (compare the continuous orange with the blue curve in Fig. 7(c)) is expected and is even targeted, given the necessary assumption of an isotropic stiffness in the FE model, which in the case of $E_p^* = E_{p,x}$ leads to an overestimation of the stiffness orthogonal to the indent. By analogy, the measured $P - h_{\text{unl}}$ curve obtained from indenting orthogonal to the extrusion direction (in the soft z-direction) is close to the model-predicted $P - h_{\text{unl}}$ curve for the case $E_p^* = E_{p,z}$, i.e. when the homogenized modulus in z-direction is considered representative for the isotropic modulus in the FE model. The measured unloading distances are slightly lower than the predicted counterparts (compare the dotdashed orange with the green curve in Fig. 7(c)), which is in line with the underestimation of the stiffness orthogonal to the indent.

All FE results presented so far refer to the Mohr–Coulomb constants $c_{\text{bm}} = 37.59$ MPa and $\varphi_{\text{bm}} = 33.14°$, which were identified from micromechanics-based downscaling of macroscopic strength tests, as discussed in Section 3.3. To further highlight the agreement between FE model and nanoindentation experiment, and to finally validate the identified constants, we now re-evaluate the FE model for the case $E_p^* = E_{p,x}$ by considering different failure constants. Reducing the cohesion to one half of the reference (while keeping the friction angle constant) leads to a significant decrease of the permanent unloading distance, see Fig. 8. The reason is that the material is more prone to plastic strains; more energy is dissipated during the loading rather than stored as elastic energy in the material, which, in turn, leads to smaller elastic strains after unloading, and thus smaller unloading distances. The agreement between the predicted $P - h_{\text{unl}}$ curve and the experimental result would thus be much worse, compare Figs. 7 and 8. Doubling the reference cohesion (while keeping the friction angle constant) leads to a significant increase of the unloading distances. While this would lead to a very close match of the experimental and modeled $P - h_{\text{unl}}$ curves for the case $E_p^* = E_{p,x}$, it would lead to a significant mismatch when comparing measurements in z-direction with model results considering $E_p^* = E_{p,z}$. Similarly to the variation of the cohesion, the model was also evaluated for varying friction angles by dividing/multiplying the friction angle by 1.3, while maintaining the reference cohesion. The resulting $P - h_{\text{unl}}$ graphs follow the aforementioned principle; a reduction of the friction angle reduces plastic but increases elastic strains and thus leads to an increase of the permanent unloading distance, and vice versa. A good fit with the nanoindentation-derived $P - h_{\text{unl}}$ curves for indentation in both x-and z- direction simultaneously, however, is not possible with any friction angle other than the reference one.

The sensitivity with respect to variations of the cohesion is less pronounced but still noticeable. This finally validates the Mohr–Coulomb failure function and the constants $c_{\text{bm}} = 37.59$ MPa, $\varphi_{\text{bm}} = 33.14°$ which are identified from micromechanics-based downscaling of macroscopic strength tests. Combining nano- and macroscale testing with micromechanics and finite element modeling, quantitative insights into brick failure at the microscale could thus be provided for the first time in brick mechanics.

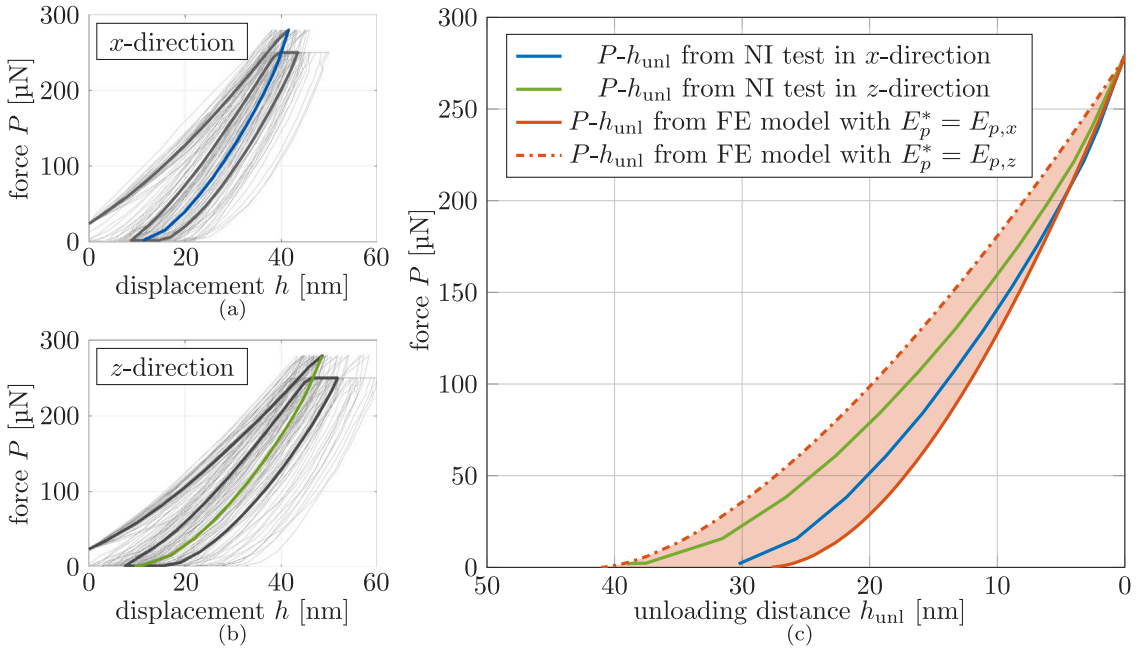

Fig. 7. Nanoindentation-derived $P - h_{\mathrm{unl}}$ curves of 40 indents related to the binding matrix in (a) x- and (b) z-direction from double-indent tests of Kariem et al. (2020a); (c) comparison of the first unloading branch of the model-predicted $P - h_{\mathrm{unl}}$ curves with nanoindentation-derived counterparts. (For interpretation of the references to color in this figure legend, the reader is referred to the web version of this article.)

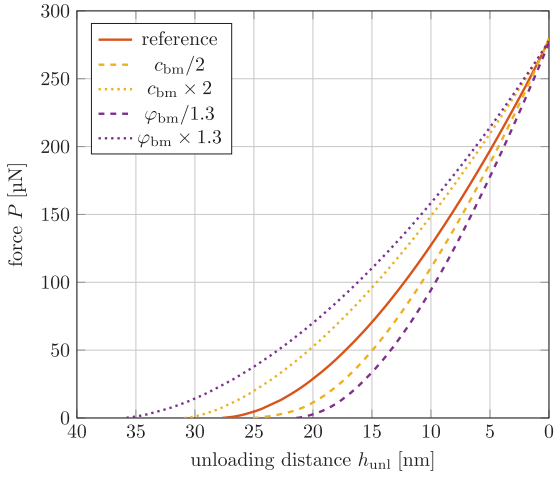

Fig. 8. Sensitivity study regarding FE model-predicted $P - h_{\mathrm{unl}}$ curves with respect to varying Mohr–Coulomb constants (reference cohesion $c_{\mathrm{bm}} = 37.59$ MPa and friction angle $\varphi_{\mathrm{bm}} = 33.14°$ according to Section 3.3.

4.2. Macrotest-based validation of the multiaxial brick failure

4.2.1. Strategy

After successful validation of the binding matrix strength constants based on nanoindentation tests, we here compare the micromechanics model predictions with published macroscopic strength data from multiaxial compression strength tests (Drobiec, 2005; Szojda, 2009; Jasiński, 2011). Microstructural information, however, is not provided by the experimenters. As a remedy, we normalize all tested multiaxial strengths by the corresponding uniaxial compressive strengths, and we normalize all predicted multiaxial strengths by the predicted uniaxial compressive strength $f_{c,x}^{\mathrm{mod}} = 74.29$ MPa. This way, we aim at checking whether micromechanics-based upscaling of the Mohr–Coulomb failure criterion (2) together with the identified and validated strength constants $c_{\mathrm{bm}} = 37.59$ MPa, $\varphi_{\mathrm{bm}} = 33.14°$ can reliably predict macroscopic brick failure under multiaxial loads.

Table 3
Results of triaxial compression tests performed by Drobiec (2005) who investigated the two loading paths A and B.

	A				B		
Σ_{xx} [MPa]	−28.4	−40.5	−48.8	−52.9	0.0	−2.0	−4.0
$\Sigma_{yy} = \Sigma_{zz}$ [MPa]	0.0	−2.1	−4.1	−6.0	−28.7	−31.3	−35.5

4.2.2. Multiaxial compression tests

A comprehensive strength test campaign was performed by Drobiec (2005) and is shortly summarized next. The authors executed triaxial compression tests on cylindrical brick specimens with a diameter of 60 mm and a height of 120 mm, with the latter dimension parallel to the extrusion direction x. Independent control of vertical stresses Σ_{xx} and radial stress $\Sigma_{yy} = \Sigma_{zz}$ allowed them to investigate two different loading paths, (A) keeping $\Sigma_{yy} = \Sigma_{zz}$ constant while Σ_{xx} is increased until failure, and (B) keeping Σ_{xx} constant while $\Sigma_{yy} = \Sigma_{zz}$ is increased until failure, see Table 3 for the stresses at failure.

Applying vertical stress Σ_{xx} only revealed that the uniaxial compressive strength amounts to $f_{c,x}^{\mathrm{Dro}} = 28.4$ MPa. The biaxial compressive strength was determined by increasing $\Sigma_{yy} = \Sigma_{zz}$, with $\Sigma_{xx} = 0$, and amounts to $f_{cc,yz}^{\mathrm{Dro}} = 28.7$ MPa. The sought bi-to-uniaxial compressive strength ratio thus amounts to $f_{cc,yz}^{\mathrm{Dro}}/f_{c,x}^{\mathrm{Dro}} = 1.01$. Jasiński (2011) also performed uniaxial and biaxial compression tests on brick cylinders with 60 mm diameter and 120 mm height. The author reported a uniaxial compressive strength of $f_{c,x}^{\mathrm{Jas}} = 23.2$ MPa and a biaxial compressive strength of $f_{cc,yz}^{\mathrm{Jas}} = 26.5$ MPa leading to a ratio of $f_{cc,yz}^{\mathrm{Jas}}/f_{c,x}^{\mathrm{Jas}} = 1.14$. Similar experiments were also carried out by Szojda (2009), who reported a bi-to-uniaxial compressive strength ratio of 0.80.

4.2.3. Micromechanics predictions of multiaxial brick failure

Evaluation of the micromechanics model for macroscopic multiaxial stress states and comparison with the aforementioned experimental results from the literature is discussed herein. In order to predict the ultimate stress at failure for any macroscopic loading $\boldsymbol{\Sigma}$, we proportionally increase the components of $\boldsymbol{\Sigma}$ in small increments, downscale the macrostresses to microstresses in the binding matrix $\boldsymbol{\sigma}_{\mathrm{bm}}$ according to

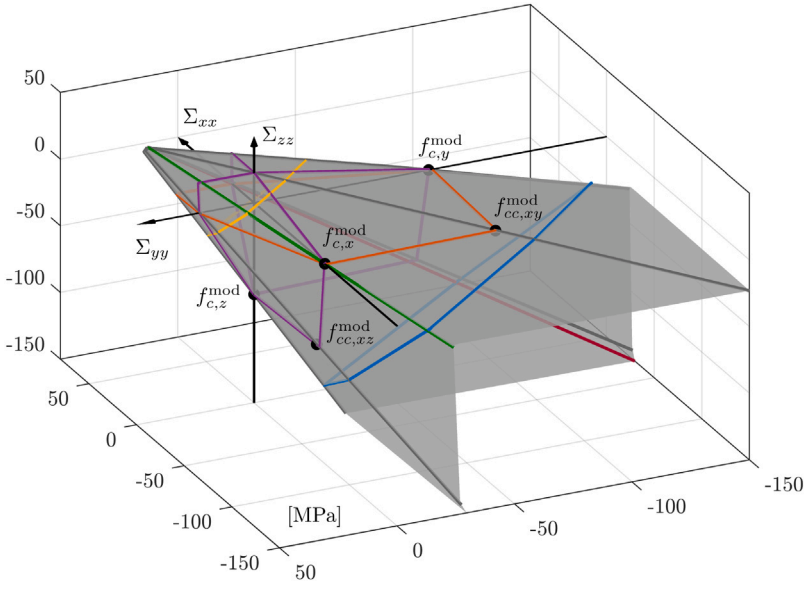

Fig. 9. Model-predicted macroscopic failure surface in principal stress space $\Sigma_{xx} - \Sigma_{yy} - \Sigma_{zz}$, with $\Sigma_{xz} = \Sigma_{yz} = \Sigma_{xy} = 0$. Biaxial sections are plotted in orange ($\Sigma_{zz} = 0$) and purple ($\Sigma_{xx} = 0$ or $\Sigma_{yy} = 0$), deviatoric sections in yellow ($\xi = 0$ MPa) and blue ($\xi = -100$ MPa), and meridians representing predictions corresponding to the experimental loading paths A and B in green ($\vartheta = 180°$) and red ($\vartheta = 0°$), respectively. (For interpretation of the references to color in this figure legend, the reader is referred to the web version of this article.)

stress concentration relation (3) and subsequently evaluate the Mohr–Coulomb failure function f_{MC} (Eq. (2)). This is repeated as long as $f_{MC}(\boldsymbol{\sigma}_{\mathrm{bm}}) < 0$. As soon as $f_{MC}(\boldsymbol{\sigma}_{\mathrm{bm}}) = 0$, the applied stress state is equal to the ultimate stress at failure.

By variation of the macroscopic load, macroscopic failure surfaces can be predicted, such as the failure surface in principal stress space (with principal stresses Σ_{xx}, Σ_{yy}, Σ_{zz} along the three axis and $\Sigma_{xz} = \Sigma_{yz} = \Sigma_{xy} = 0$), depicted in Fig. 9. Any macroscopic loading leading to stress states which are located inside the failure surface, i.e. between the surface and the hydrostatic axis $\Sigma_{xx} = \Sigma_{yy} = \Sigma_{zz}$, is tolerated by the brick. Failure occurs once the macrostresses fall at the surface. Notably, the failure surface exhibits the shape of a five-sided pyramid, which is very close to a Mohr–Coulomb failure surface, see also the deviatoric section in Haigh–Westergaard coordinates (with ξ as hydrostatic coordinate, r as deviatoric coordinate, and ϑ as Lode angle) depicted in Fig. 10. Unlike the deviatoric sections through the predicted failure surface are not symmetric with respect mirroring along $\vartheta = 0$ or $\vartheta = 2\pi/3$. Given the axisymmetrical microstructure with symmetry axis z, the uniaxial compressive as well as tensile strengths in x- and y-direction ($f_{c,x}^{\mathrm{mod}} = f_{c,y}^{\mathrm{mod}} = 74.29$ MPa, $f_{t,x}^{\mathrm{mod}} = f_{t,y}^{\mathrm{mod}} = 23.10$ MPa) are slightly larger than those in z-direction ($f_{c,z}^{\mathrm{mod}} = 68.70$ MPa, $f_{t,z}^{\mathrm{mod}} = 22.18$ MPa). We note that microstructures with larger asphericities of mineral and pore phases and/or more pronounced orientation distributions, as compared to the studied reference brick, lead to larger asymmetries of the failure surfaces.

Moreover, we study shear failure surfaces. Failure surfaces in the $\Sigma_{xx} - \Sigma_{yy} - \Sigma_{xy}$ stress space (with $\Sigma_{zz} = \Sigma_{xz} = \Sigma_{yz} = 0$) in Fig. 11(a) is very similar to the $\Sigma_{xx} - \Sigma_{zz} - \Sigma_{xz}$ failure surface (with $\Sigma_{yy} = \Sigma_{xy} = \Sigma_{yz} = 0$). For interpretation, we focus on symmetric biaxial stress states $\Sigma_{xx} = \Sigma_{yy}$ in Fig. 11(a). As the symmetric biaxial stress decreases (the compression increases), the transmittable shear stress also increases and reaches its maximum at $\Sigma_{xx} = \Sigma_{yy} = f_{c,x}^{\mathrm{mod}}/2$. If the biaxial compression is further increased, the transmittable shear stress decreases and reaches zero at the biaxial strength $f_{cc,xy}^{\mathrm{mod}}$. The intersections of the vertical axes with the failure surfaces represent the predicted brick shear strengths, $f_{s,xy}^{\mathrm{mod}} = 17.6$ MPa and $f_{s,xz}^{\mathrm{mod}} = f_{s,yz}^{\mathrm{mod}} = 17.4$ MPa, respectively. The difference between the two is caused by the transversal isotropic characteristic of the brick.

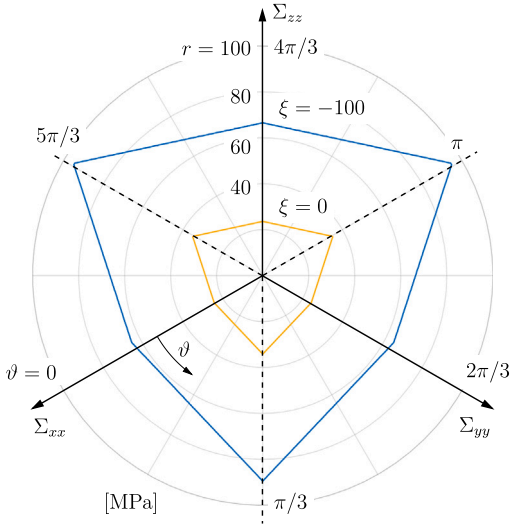

Fig. 10. Deviatoric section through the failure surface of Fig. 9 at the different hydrostatic pressures $\xi = 0$ MPa and $\xi = -100$ MPa.

4.2.4. Comparison and validation

As for validation of the micromechanics model, the bi- and triaxial test results, discussed in Section 4.2.2, are compared with the corresponding model predictions, presented in Section 4.2.3. For comparison of the triaxial compression test results from Drobiec (2005), failure stresses for both loading paths are transformed from Cartesian components Σ_{xx}, Σ_{yy}, and Σ_{zz}, given in Table 3, to Haigh–Westergaard coordinates ξ, r, ϑ. Loading path A refers to Lode angles $\vartheta = 180°$ and is therefore compared to the model-predicted *compressive* meridian, compare the green points to the green line in Fig. 12. Loading path B, in turn, refers to Lode angles $\vartheta = 0°$ and is therefore compared to the model-predicted *tensile* meridian, compare the red points to the red line in Fig. 12. The agreement between the normalized failure stresses for both loading paths is excellent.

Finally, biaxial compression tests from Drobiec (2005), Szojda (2009) and Jasiński (2011) are compared to the corresponding

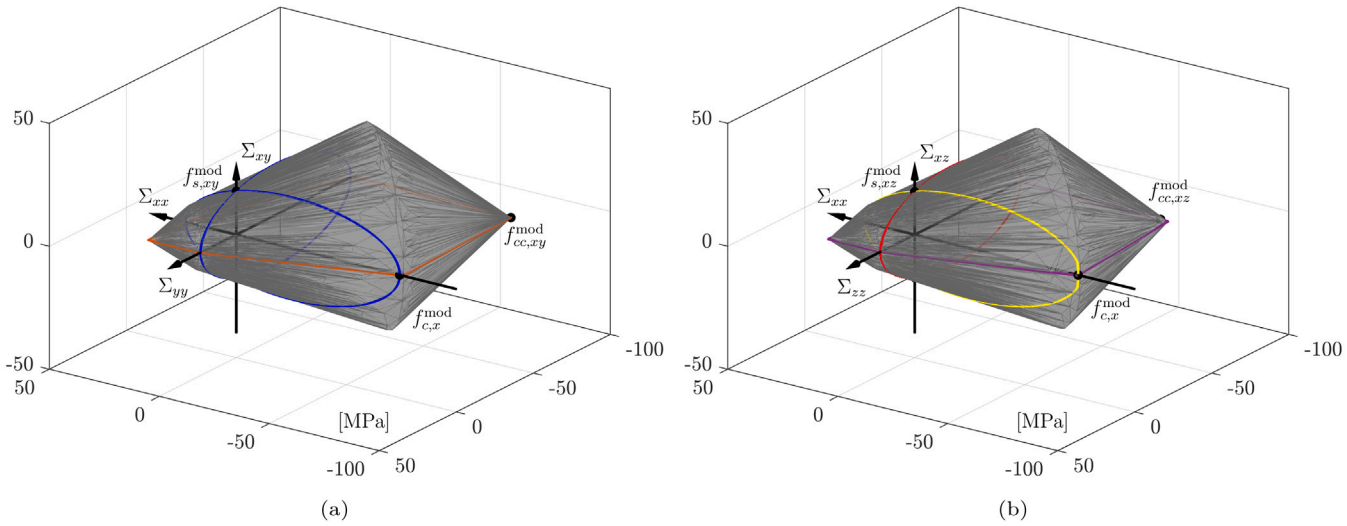

Fig. 11. Model-predicted macroscopic failure surfaces: (a) $\Sigma_{xx} - \Sigma_{yy} - \Sigma_{xy}$ stress space with $\Sigma_{zz} = \Sigma_{xz} = \Sigma_{yz} = 0$; (b) $\Sigma_{xx} - \Sigma_{zz} - \Sigma_{xz}$ stress space with $\Sigma_{yy} = \Sigma_{xy} = \Sigma_{yz} = 0$. The intersections of surface and vertical axis represent the brick shear strengths $f^{\mathrm{mod}}_{s,xy}$ and $f^{\mathrm{mod}}_{s,xz}$.

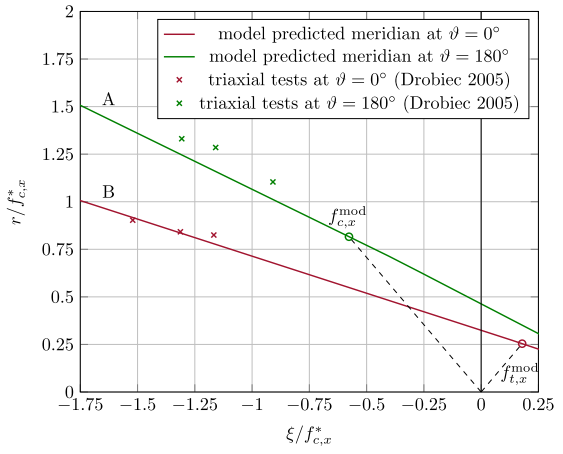

Fig. 12. Comparison of model-predicted failure meridians in principal stress space ($r-\xi$-diagram) with experimentally measured failure stresses from triaxial compression tests of Drobiec (2005) for two loading paths A and B. Predicted stresses are normalized by the predicted uniaxial compressive strength ($f^{*}_{c,x} = f^{\mathrm{mod}}_{c,x}$) and measured stresses are normalized by the measured uniaxial compressive strength ($f^{*}_{c,x} = f^{\mathrm{Dro}}_{c,x}$). (For interpretation of the references to color in this figure legend, the reader is referred to the web version of this article.)

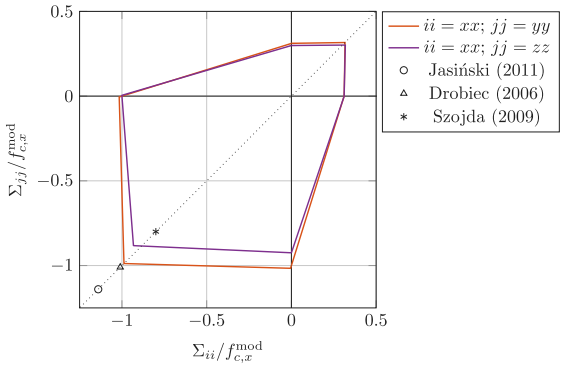

Fig. 13. Model-predicted normalized biaxial failure surface in the $\Sigma_{xx} - \Sigma_{yy}$ plane with $\Sigma_{zz} = \Sigma_{xz} = \Sigma_{yz} = \Sigma_{xy} = 0$ (orange) and the $\Sigma_{xx} - \Sigma_{zz}$ plane with $\Sigma_{yy} = \Sigma_{xz} = \Sigma_{yz} = \Sigma_{xy} = 0$ or the $\Sigma_{yy} - \Sigma_{zz}$ plane with $\Sigma_{xx} = \Sigma_{xz} = \Sigma_{yz} = \Sigma_{xy} = 0$ (purple), and comparison with experimentally determined biaxial-to-uniaxial compressive strength ratios. (For interpretation of the references to color in this figure legend, the reader is referred to the web version of this article.)

model predictions. The experimentally determined biaxial-to-uniaxial compressive strength ratios are close to one, and thus also agree very well with the corresponding modeled ratio amounting to $f^{\mathrm{mod}}_{cc,yz}/f^{\mathrm{mod}}_{c,x} = 65.72/74.29 = 0.88$, see Fig. 13 for a graphical illustration based on the predicted biaxial failure surfaces.

5. Summary, conclusions and outlook

In this work, we aim at modeling the strength of extruded fired (880 °C) clay brick by means of a continuum micromechanics approach. Therefore, the complex microstructure of bricks, consisting of several mineral phases as well as pores at several length scales, is resolved down to the scale of micrometers where a vitrified binding matrix is considered. Brick failure is associated to Mohr–Coulomb-type failure of this matrix, with strength constants obtained from downscaling macroscopic tensile and compressive brick strength tests. The scale transitions required for this downscaling, as well as for upscaling of the microscopic binding matrix strength to the macroscopic brick scale, are provided by micromechanics-derived stress concentration relations, relying on the microstructural representation.

Model validation is successfully achieved at both the microscale and the macroscale. The strength constants of the microscopic binding matrix are validated by comparing finite element results which rely on the identified failure behavior to unloading curves obtained from nanoindentation experiments (Kariem et al., 2020a). The predicted multiaxial brick strength is compared to independent results from triaxial and biaxial compression tests (Drobiec, 2005; Jasiński, 2011; Szojda, 2009). For the first time in brick mechanics, the model establishes a microstructure-based quantitative link between microscopic and macroscopic failure. At this point, it should be noted that the authors are aware of the complexity of failure mechanisms in brick materials and that the proposed model cannot fully describe reality. However, the presented identification of strength properties of the binding matrix provides a first mechanically sound estimate of the magnitude of these, which should be a reasonable basis for further developments.

The proposed micromechanics multiscale model is currently limited to one type of clay brick fired at 880 °C. Extending the applicability to different clays, different firing temperatures, as well as mixtures with pore-forming additives (e.g. extruded polystyrene, saw dust, and paper

sludge) or tempers (e.g. fly ash, slag, and quartz sand) is a challenging but fertile task for future modeling attempts. A preliminary application to different clay mixtures has already shown that their macroscopic strengths can be predicted reliably, which will be presented in a follow-up publication. The focus will be, on the one hand, on a detailed investigation of the mechanical properties of the binding matrix as a function of mineralogical brick composition and firing temperature, and, on the other hand, on the investigation of structural changes in the brick material due to the addition of pore-forming additives and tempers. The microstructure observations should be combined with macroscopic strength tests in order to validate the micro–macro link provided by the model. This would finally allow revealing the full potential of a micromechanics multiscale model: to quantitatively study the brick strength and its sensitivity with respect to changes in composition or production and to provide a scientific basis for optimizing existing bricks and developing new ones.

Declaration of competing interest

The authors declare that they have no known competing financial interests or personal relationships that could have appeared to influence the work reported in this paper.

Acknowledgments

The authors gratefully acknowledge the financial support of the Austrian Research Promotion Agency (FFG, project number 865067), the "Klima- und Energiefonds" Austria, and the industry partner Wienerberger AG for funding the research work through the project 'Innovative Brick 2'. Furthermore, the authors acknowledge TU Wien Bibliothek for financial support through its Open Access Funding Programme, and would like to thank Hawraa Kariem for providing the results of an extensive grid nanoindentation on fired clay bricks.

References

Allegretta, I., Eramo, G., Pinto, D., Hein, A., 2017. The effect of mineralogy, microstructure and firing temperature on the effective thermal conductivity of traditional hot processing ceramics. Appl. Clay Sci. 135, 260–270. http://dx.doi.org/10.1016/j.clay.2016.10.001.

Bader, T.K., Hofstetter, K., Hellmich, C., Eberhardsteiner, J., 2010. Poromechanical scale transitions of failure stresses in wood: from the lignin to the spruce level. J. Appl. Math. Mech. 90 (10–11), 750–767. http://dx.doi.org/10.1002/zamm.201000045.

Bartusch, R., Händle, F., 2007. In: Händle, F. (Ed.), Extrusion in Ceramics. Springer-Verlag.

Benveniste, Y., 1987. A new approch to the application of Mori-Tanaka's theory in composite materials. Mech. Mater. 6, 147–157. http://dx.doi.org/10.1016/0167-6636(87)90005-6.

Bourret, J., Tessier-Doyen, N., Guinebretiere, R., Joussein, E., Smith, D.S., 2015. Anisotropy of thermal conductivity and elastic properties of extruded clay-based materials: Evolution with thermal treatment. Appl. Clay Sci. 116–117, 150–157. http://dx.doi.org/10.1016/j.clay.2015.08.006.

Brinell, J.A., 1901. The hardness of metals. In: Congres International des Methodes d'Essai des Materiaux de Construction, Vol. 2. pp. 83–94.

Buchner, T., Kiefer, T., Gaggl, W., Zelaya-Lainez, L., Füssl, J., 2021a. Automated morphometrical characterization of material phases of fired clay bricks based on Scanning Electron Microscopy, Energy Dispersive X-ray Spectroscopy and Powder X-ray Diffraction. Constr. Build. Mater. (ISSN: 0950-0618) 288, 122909. http://dx.doi.org/10.1016/j.conbuildmat.2021.122909, URL https://www.sciencedirect.com/science/article/pii/S0950061821006693.

Buchner, T., Kiefer, T., Königsberger, M., Jäger, A., Füssl, J., 2021b. Continuum micromechanics model for fired clay bricks: Upscaling of experimentally identified microstructural features to macroscopic elastic stiffness and thermal conductivity. Mater. Des. (ISSN: 0264-1275) 212, 110212. http://dx.doi.org/10.1016/j.matdes.2021.110212, URL https://www.sciencedirect.com/science/article/pii/S026412752100767X.

Buchner, T., Kiefer, T., Zelaya-Lainez, L., Gaggl, W., Konegger, T., Füssl, J., 2021c. A multitechnique, quantitative characterization of the pore space of fired bricks made of five clayey raw materials used in European brick industry. Appl. Clay Science (ISSN: 0169-1317) 200, 105884. http://dx.doi.org/10.1016/j.clay.2020.105884, URL https://www.sciencedirect.com/science/article/pii/S016913172030449X.

Chapagain, Y., Sapkota, S., Ghale, D., Bohara, N., Duwal, N., Bhattarai, J., 2020. Characterization of mechanical properties of polymers by nanoindentation tests. Nepal SN Appl. Sci. 2, 1856. http://dx.doi.org/10.1007/s42452-020-03535-y.

Chen, X., Xiang, Y., Vlassak, J., 2006. Novel technique for measuring the mechanical properties of porous materials by nanoindentation. J. Mater. Res. 21, 715–724. http://dx.doi.org/10.1557/jmr.2006.0088, URL https://link.springer.com/article/10.1557/jmr.2006.0088.

Christensen, N.I., 1996. Poisson's ratio and crustal seismology. J. Geol. Res. 101 (B2), 3139–3156. http://dx.doi.org/10.1029/95JB03446.

Coletti, C., Cultrone, G., Maritana, L., Mazzoli, C., 2016a. Combined multi-analytical approach for study of pore system in bricks: How much porosity is there? Mater. Charact. 121, 80–92. http://dx.doi.org/10.1016/j.matchar.2016.09.024.

Coletti, C., Cultrone, G., Maritana, L., Mazzoli, C., 2016b. How to face the new industrial challenge of compatible, sustainable brick production: Study of various types of commercially available bricks. Appl. Clay Sci. 124–125, 219–226. http://dx.doi.org/10.1016/j.clay.2016.02.014.

Constantinides, G., Ulm, F.-J., Vliet, K.V., 2003. On the use of nanoindentation for cementitious materials. Mater. Struct. 36, 191–196. http://dx.doi.org/10.1007/BF02479557.

D'Orazio, M., Lenci, S., Graziani, L., 2014. Relationship between fracture toughness and porosity of clay brick panels used in ventilated façades: Initial investigation. Eng. Fract. Mech. 116, 108–121. http://dx.doi.org/10.1016/j.engfracmech.2013.12.003.

Dormieux, L., Kondo, D., Ulm, F.-J., 2006. Microporomechanics. John Wiley & Sons, http://dx.doi.org/10.1002/0470032006.

Drobiec, L., 2005. FEM micro-model of masonry. In: 5th International Conference AMCM 2005. URL https://www.researchgate.net/publication/328880672_FEM_micro_model_of_masonry.

Drugan, W., Willis, J., 1996. A micromechanics-based nonlocal constitutive equation and estimates of representative volume element size for elastic composites. J. Mech. Phys. Solids (ISSN: 0022-5096) 44 (4), 497–524. http://dx.doi.org/10.1016/0022-5096(96)00007-5, URL https://www.sciencedirect.com/science/article/pii/0022509696000075.

Eshelby, J.D., 1957. The determination of the elastic field of an ellipsoidal inclusion, and related problems. Proc. R. Soc. Lond. Ser. A Math. Phys. Eng. Sci. 241 (1226), 376–396.

Gangwar, T., Schillinger, D., 2019. Microimaging-informed continuum micromechanics accurately predicts macroscopic stiffness and strength properties of hierarchical plant culm materials. Mech. Mater. (ISSN: 0167-6636) 130, 39–57. http://dx.doi.org/10.1016/j.mechmat.2019.01.009, URL https://www.sciencedirect.com/science/article/pii/S0167663618305763.

Ganneau, F.P., Constantinides, G., Ulm, F.-J., 2006. Dual-indentation technique for the assessment of strength properties of cohesive-frictional materials. Int. J. Solids Struct. 43, 1727–1745. http://dx.doi.org/10.1016/j.ijsolstr.2005.03.035.

Ganz, H., 1985. Mauerwerksscheiben unter Normalkraft und Schub (Ph.D. thesis). Eidgenössische Technische Hochschule Zürich, http://dx.doi.org/10.3929/ethz-a-000360363.

Grandjean, S., Absi, J., Smith, D., 2006. Numerical calculations of the thermal conductivity of porous ceramics based on micrographs. J. Eur. Ceram. Soc. (ISSN: 0955-2219) 26 (13), 2669–2676. http://dx.doi.org/10.1016/j.jeurceramsoc.2005.07.061, URL http://www.sciencedirect.com/science/article/pii/S0955221905007478.

Graubner, C., Richter, L., 2007. Diskrete FE-modellierung von mauerwerk zur bestimmung der druckfestigkeit. Mauerwerk 11, 342–348. http://dx.doi.org/10.1002/dama.200700354.

Hill, R., 1963. Elastic properties of reinforced solids: some theoretical principles. J. Mech. Phys. Solids 11, 357–372. http://dx.doi.org/10.1016/0022-5096(63)90036-X.

Hill, R., 1965. Continuum micro-mechanics of elastoplastic polycrystals. J. Mech. Phys. Solids 13 (2), 89–101. http://dx.doi.org/10.1016/0022-5096(65)90023-2.

Hofstetter, K., Hellmich, C., Eberhardsteiner, J., Mang, H., 2008. Miromechanical estimates for elastic limit states in wood materials revealing nanostructural failure mechanisms. Mech. Adv. Mater. Struct. 15, 474–484. http://dx.doi.org/10.1080/15376490802142387.

Hřibalová, S., Uhlířová, T., Pabst, W., 2021. Computer modeling of systematic processing defects on the thermal and elastic properties of open Kelvin-cell metamaterials. J. Eur. Ceram. Soc. (ISSN: 0955-2219) 41 (14), 7130–7140. http://dx.doi.org/10.1016/j.jeurceramsoc.2021.07.031, URL https://www.sciencedirect.com/science/article/pii/S095522192100501X.

Igarashi, S., Bentur, A., Mindess, S., 1996. Characterization of the microstructure and strength of cement paste by microhardness testing. Adv. Cem. Res. 8, 87–92. http://dx.doi.org/10.1680/adcr.1996.8.30.87.

Jasiński, R., 2011. Numerical model of the horizontally sheared wall. In: Conference: Analytical Models and New Concepts in Concrete and Masonry Structures. URL https://www.researchgate.net/publication/307954526_NUMERICAL_MODEL_OF_THE_HORIZONTALLY_SHEARED_WALL.

Kariem, H., Füssl, J., Kiefer, T., Jäger, A., Hellmich, C., 2020a. The viscoelastic behaviour of material phases in fired clay identified by means of grid nanoindentation. Constr. Build. Mater. (ISSN: 0950-0618) 231, 117066. http://dx.doi.org/10.1016/j.conbuildmat.2019.117066, URL http://www.sciencedirect.com/science/article/pii/S0950061819325085.

Kariem, H., Hellmich, C., Kiefer, T., Jäger, A., Füssl, J., 2018. Micro-CT-based identification of double porosity in fired clay ceramics. J. Mater. Sci. (ISSN: 1573-4803) 53 (13), 9411–9428. http://dx.doi.org/10.1007/s10853-018-2281-9.

Kariem, H., Kiefer, T., Hellmich, C., Gaggl, W., Steiger-Thirsfeld, A., Füssl, J., 2020b. EDX/XRD-based identification of micrometer-sized domains in scanning electron micrographs of fired clay. Mater. Struct. 53 (109), http://dx.doi.org/10.1617/s11527-020-01531-7.

Kermouche, G., Barthel, E., Vandembroucq, D., Dubujet, P., 2008. Mechanical modelling of indentation-induced densification in amorphous silica. Acta Mater. (ISSN: 1359-6454) 56 (13), 3222–3228. http://dx.doi.org/10.1016/j.actamat.2008.03.010, URL https://www.sciencedirect.com/science/article/pii/S1359645408001997.

Kholmyansky, M., Kogan, E., Kovler, K., 1994. On the hardness determination of fine-grained concrete. Mater. Struct. 27, 584–587. http://dx.doi.org/10.1007/BF02473127.

Kiefer, T., Füssl, J., Kariem, H., Konnerth, J., Gaggl, W., Hellmich, C., 2020. A multi-scale material model for the estimation of the transversely isotropic thermal conductivity tensor of fired clay bricks. J. Eur. Ceram. Soc. (ISSN: 0955-2219) 40 (15), 6200–6217. http://dx.doi.org/10.1016/j.jeurceramsoc.2020.05.018, URL https://www.sciencedirect.com/science/article/pii/S0955221920303691.

Kiefer, T., Kariem, H., Lukacevic, M., Füssl, J., 2017. The compressive strength of vertically perforated clay block masonry predicted by means of a unit-cell type numerical simulation tool taking discrete cracking into account. Constr. Build. Mater. (ISSN: 0950-0618) 150, 24–34. http://dx.doi.org/10.1016/j.conbuildmat.2017.05.201, URL https://www.sciencedirect.com/science/article/pii/S0950061817310991.

Kilikoglou, V., Vekinis, G., Maniatis, Y., 1995. Toughening of ceramic earthenwares by quartz inclusions: AN ancient art revisited. Acta Metall. Mater. 43 (8), 2959–2965. http://dx.doi.org/10.1016/0956-7151(95)00006-H.

Kilikoglou, V., Vekinis, G., Maniatis, Y., Day, P.M., 1998. Mechanical performance of quartz-tempered ceramics: Part I strength and toughness. Archaeometry 40 (2), 261–279. http://dx.doi.org/10.1111/j.1475-4754.1998.tb00837.x.

Kohlhauser, C., Hellmich, C., 2013. Ultrasonic contact pulse transmission for elastic wave velocity and stiffness determination: Influence of specimen geometry and porosity. Eng. Struct. 47, 115–133. http://dx.doi.org/10.1016/j.engstruct.2012.10.027.

Königsberger, M., Hlobil, M., Delsaute, B., Staquet, S., Hellmicha, C., Pichler, B., 2018. Hydrate failure in ITZ governs concrete strength: A micro-to-macro validated engineering mechanics model. Cem. Concr. Res. 103, 77–94. http://dx.doi.org/10.1016/j.cemconres.2017.10.002.

Königsberger, M., Pichler, B., Hellmich, C., 2014a. Micromechanics of ITZ–aggregate interaction in concrete part I: Stress concentration. J. Am. Ceram. Soc. 97 (2), 535–542. http://dx.doi.org/10.1111/jace.12591.

Königsberger, M., Pichler, B., Hellmich, C., 2014b. Micromechanics of ITZ-aggregate interaction in concrete part II: Strength upscaling. J. Am. Ceram. Soc. 97 (2), 543–551. http://dx.doi.org/10.1111/jace.12606.

Königsberger, M., Pichler, B., Hellmich, C., 2020. Multiscale poro-elasticity of densifying calcium-silicate hydrates in cement paste: An experimentally validated continuum micromechanics approach. Internat. J. Engrg. Sci. (ISSN: 00207225) 147, http://dx.doi.org/10.1016/j.ijengsci.2019.103196.

Königsberger, M., Staquet, S., 2018. Micromechanical multiscale modeling of ITZ-driven failure of recycled concrete: Effects of composition and maturity on the material strength. Appl. Sci. 8 (6), 976. http://dx.doi.org/10.3390/app8060976.

Krakowiak, K.J., Lourenço, P.B., Ulm, F.-J., 2011. Multitechnique investigation of extruded clay brick microstructure. J. Am. Ceram. Soc. 94 (9), 3012–3022. http://dx.doi.org/10.1111/j.1551-2916.2011.04484.

Lourenço, P., 1997. Computational Strategies for Masonry Structures (Ph.D. thesis). Delft University of Technology.

Lourenço, P., Vasconcelos, G., 2015. 2 - The design and mechanical performance of high-performance perforated fired masonry bricks. In: Pacheco-Torgal, F., Lourenço, P., Labrincha, J., Kumar, S., Chindaprasirt, P. (Eds.), Eco-Efficient Masonry Bricks and Blocks. Woodhead Publishing, Oxford, ISBN: 978-1-78242-305-8, pp. 13–44. http://dx.doi.org/10.1016/B978-1-78242-305-8.00002-4, URL https://www.sciencedirect.com/science/article/pii/B9781782423058000024.

Menétrey, P., Willam, K.J., 1995. Triaxial failure criterion for concrete and its generalization. ACI Struct. J. 92 (3), http://dx.doi.org/10.14359/1132.

Mori, T., Tanaka, K., 1973. Average stress in matrix and average elastic energy of materials with misfitting inclusions. Acta Metall. (ISSN: 0001-6160) 21 (5), 571–574. http://dx.doi.org/10.1016/0001-6160(73)90064-3, URL https://www.sciencedirect.com/science/article/pii/0001616073900643.

Müller, N.S., Kilikoglou, V., Day, P.M., Vekinis, G., 2010. The influence of temper shape on the mechanical properties of archaeological ceramics. J. Eur. Ceram. Soc. 30, 2457–2465. http://dx.doi.org/10.1016/j.jeurceramsoc.2010.04.039.

Müller, N.S., Vekinis, G., Day, P., Kilikoglou, V., 2015. The influence of microstructure and texture on the mechanical properties of rock tempered archaeological ceramics. J. Eur. Ceram. Soc. 35, 831–843. http://dx.doi.org/10.1016/j.jeurceramsoc.2014.09.025.

Mura, T., 1987. Micromechanics of Defects in Solids, Vol. 3. Springer.

Nežerka, V., Zeman, J., Němeček, J., 2017. Micromechanics-based simulations of compressive and tensile testing on lime-based mortars. Mech. Mater. (ISSN: 0167-6636) 105, 49–60. http://dx.doi.org/10.1016/j.mechmat.2016.11.011, URL https://www.sciencedirect.com/science/article/pii/S0167663616305348.

Nguyen, T.-D., Meftah, F., 2014. Behavior of hollow clay brick masonry walls during fire. Part 2: 3D finite element modeling and spalling assessment. Fire Saf. J. (ISSN: 0379-7112) 66, 35–45. http://dx.doi.org/10.1016/j.firesaf.2013.08.017, URL https://www.sciencedirect.com/science/article/pii/S037971121300180X.

Oliver, W.C., Pharr, G.M., 1992. An improved technique for determining hardness and elastic modulus using load and displacement sensing indentation experiments. J. Mater. Res. 7, 1564–1583. http://dx.doi.org/10.1557/JMR.1992.1564.

Oliver, W., Pharr, G., 2004. Measurement of hardness and elastic modulus by instrumented indentation: advances in understanding and refinements to methodology. J. Mater. Res. 19 (1), 3–20. http://dx.doi.org/10.1557/jmr.2004.19.1.3.

Pabst, W., Gregorová, E., 2007. A cross-property relation between the tensile modulus and the thermal conductivity of porous materials. Ceram. Int. 33, 9–12. http://dx.doi.org/10.1016/j.ceramint.2005.07.009.

Pabst, W., Gregorová, E., 2017. A generalized cross-property realtion between the elastic moduli and conductivity of isotropic porous materials with spheroidal pores. Ceramics-Silikáty 61 (1), 74–80. http://dx.doi.org/10.13168/cs.2016.0063.

Pabst, W., Uhlířová, T., 2021. Benchmark polynomials for the porosity dependence of elastic moduli and conductivity of partially sintered ceramics. J. Eur. Ceram. Soc. (ISSN: 0955-2219) http://dx.doi.org/10.1016/j.jeurceramsoc.2021.08.028, URL https://www.sciencedirect.com/science/article/pii/S0955221921005951.

Pichler, B., Hellmich, C., 2011. Upscaling quasi-brittle strength of cement paste and mortar: A multi-scale engineering mechanics model. Cem. Concr. Res. 41 (5), 467–476. http://dx.doi.org/10.1016/j.cemconres.2011.01.010.

Pichler, C., Traxl, R., Lackner, R., 2015. Power-law scaling of thermal conductivity of highly porous ceramics. J. Eur. Ceram. Soc. (ISSN: 0955-2219) 35 (6), 1933–1941. http://dx.doi.org/10.1016/j.jeurceramsoc.2014.12.004, URL http://www.sciencedirect.com/science/article/pii/S095522191400661X.

Sarris, E., Constantinides, G., 2013. Finite element modeling of nanoindentation on CSH: Effect of pile-up and contact friction. Cem. Concr. Compos. 36, 78–84. http://dx.doi.org/10.1016/j.cemconcomp.2012.10.010.

Sevostianov, I., Kachanov, M., 2014. On some controversial issues in effective field approaches to the problem of the overall elastic properties. Mech. Mater. (ISSN: 0167-6636) 69 (1), 93–105. http://dx.doi.org/10.1016/j.mechmat.2013.09.010, URL https://www.sciencedirect.com/science/article/pii/S0167663613001853.

Suda, R., Kiefer, T., Schranz, C., Füssl, J., 2021. A finite-element-based approach to quantify the impact of bed joint reinforcement on the compressive strength of vertically perforated clay block masonry. Eng. Struct. (ISSN: 0141-0296) 239, 112277. http://dx.doi.org/10.1016/j.engstruct.2021.112277, URL https://www.sciencedirect.com/science/article/pii/S0141029621004272.

Suquet, P., 1997. Continuum Micromechanics. In: CISM Courses and Lectures, vol. 377, Springer Verlag.

Szojda, L., 2009. Analiza Numeryczna Wplywu Nieciaglych Deformacji Podloza na Budynki Ścianowe. Wydawnictwo Politechniki Ślaskiej, Gliwice.

Tabor, D., 1951. The hardness of metals. In: Congres International des Methodes d'Essai des Materiaux de Construction, Edition 2000.

Uhlířová, T., Nečina, V., Pabst, W., 2018. Modeling of Young's modulus and thermal conductivity evolution of partially sintered alumina ceramics with pore shape changes from concave to convex. J. Eur. Ceram. Soc. (ISSN: 0955-2219) 38 (8), 3004–3011. http://dx.doi.org/10.1016/j.jeurceramsoc.2017.12.033, URL https://www.sciencedirect.com/science/article/pii/S0955221917308439. Cermodel 2017: Modelling and Simulation Meet Innovation in Ceramics Technology.

VanLandingham, M.R., Villarrubia, J.S., Guthrie, W.F., Meyers, G.F., 2001. Nanoindentation of polymers: An overview. Macromol. Symp. 167, 15–43. http://dx.doi.org/10.1002/1521-3900(200103)167:1<15::AID-MASY15>3.0.CO;2-T.

Wagh, A.S., Singh, J.P., Poeppel, R.B., 1993. Dependence of ceramic fracture properties on porosity. J. Mater. Sci. 28, 3589–3593. http://dx.doi.org/10.1007/BF01159841.

Williams, S.R., 1942. Hardness and hardness measurements. Am. Soc. Met..

Zaoui, A., 2002. Continuum micromechanics: Survey. J. Eng. Mech. 128 (2), 808–816. http://dx.doi.org/10.1061/(asce)0733-9399(2002)128:8(808).

Zhang, C., Zhang, Y., Zeng, K., Shen, L., 2006a. Characterization of mechanical properties of polymers by nanoindentation tests. Phil. Mag. 86 (28), 4487–4506. http://dx.doi.org/10.1080/14786430600735476.

Zhang, C., Zhang, Y., Zeng, K., Shen, L., Wang, Y., 2006b. Extracting the elastic and viscoelastic properties of a polymeric film using a sharp indentation relaxation test. J. Mater. Res. 21 (12), 2991–3000. http://dx.doi.org/10.1557/JMR.2006.0395.

Živcová, Z., Černý, M., Pabst, W., Gregorová, E., 2009a. Elastic properties of porous oxide ceramics prepared using starch as a pore-forming agent. J. Eur. Ceram. Soc. (ISSN: 0955-2219) 29 (13), 2765–2771. http://dx.doi.org/10.1016/j.jeurceramsoc.2009.03.033, URL http://www.sciencedirect.com/science/article/pii/S0955221909001496.

Živcová, Z., Gregorová, E., Pabst, W., Smith, D.S., Michot, A., Poulier, C., 2009b. Thermal conductivity of porous alumina ceramics prepared using starch as a pore-forming agent. J. Eur. Ceram. Soc. (ISSN: 0955-2219) 29 (3), 347–353. http://dx.doi.org/10.1016/j.jeurceramsoc.2008.06.018, URL http://www.sciencedirect.com/science/article/pii/S0955221908003233.